ARTICLE IN PRESS

Available online at www.sciencedirect.com

SCIENCE DIRECT®

Comput. Methods Appl. Mech. Engrg. xxx (2005) xxx–xxx

Computer methods in applied mechanics and engineering

www.elsevier.com/locate/cma

Multidimensional modelling for the carotid artery blood flow

S.A. Urquiza [a], P.J. Blanco [a,c], M.J. Vénere [b], R.A. Feijóo [c,*]

[a] Laboratorio de Bioingeniería, Universidad Nacional de Mar del Plata, Av. J.B. Justo 4302, 7600 Mar del Plata, Argentina
[b] PLADEMA—CNEA, Facultad de Exactas, Universidad Nacional del Centro de la Provincia de Buenos Aires, Pinto 399, 7000 Tandil, Argentina
[c] L.N.C.C., Laboratório Nacional de Computação Científica, Av. Getulio Vargas 333, Quitandinha, 25651-075, Petrópolis, RJ, Brazil

Received 18 March 2004; accepted 26 July 2005

Abstract

In this work, a multidimensional 3D–1D FEM model of the whole arterial tree is implemented. It comprises a 3D compliant model of the carotid bifurcation coupled with a 1D model for the remaining part of the arterial tree. With this approach, difficulties arising from the treatment of boundary conditions for the 3D model are naturally handled. The Navier–Stokes equations are used as the governing equations for the blood flow while an elastic compliant model is implemented for the arterial wall. Also, the A.L.E. formulation is considered within the 3D blood regions taking into account the domain deformations produced by the moving artery wall. This 3D model is complemented with a 1D model of the entire arterial tree, in order to appropriately set inflow and outflow boundary conditions for the former. The reduced 1D model solves the momentum and continuity equations in compliant tubes so as to reproduce the propagation of the pressure pulse in the arterial network. Also, a volumetric flow rate is imposed at the inlet to model the systolic work of the heart. The peripheral arteriole beds are simulated with the well-known lumped Windkessel model. A standard geometry of the carotid bifurcation is discretized with P1 bubble–P1 tetrahedral elements. The obtained results properly reproduce the general flow patterns reported in the literature. Very good agreement between the outcomes of a pure 1D model and those of the combined multidimensional model was obtained. It is worth noting that this kind of model may provide useful information to gain understanding in the genesis and development of arterial diseases.

Keywords: Hemodynamic; Fluid–structure interaction; FEM; Coupling 3D–1D

1. Introduction

Arterial vessel trees perform the vital task of efficiently supplying blood to all organs and tissues of the body, carrying nutrients and removing catabolic products. Hemodynamic simulation studies have been frequently used to gain a better understanding of functional, diagnostic and therapeutic aspects of the blood flow. These simulations usually employ compartmental representations or branching tube models of arterial trees as their geometrical substrate [1,28–31,33]-specially to model large extended zones—whereas localized three-dimensional models have been often implemented to study arterial flow in more detailed aspects [3,7,20,27,35].

Blood flow studies in the carotid artery bifurcation are of great clinical interest with respect to both, the genesis and the diagnostics of atherosclerotic diseases. It is well known [13] that the flow separation region of the carotid sinus has the propensity to develop atherosclerotic plaques. In this sense, the local hemodynamic structure is intimately related to

---

[*] Corresponding author.
E-mail addresses: santiagourquiza@fi.mdp.edu.ar (S.A. Urquiza), venerem@exa.unicen.edu.ar (M.J. Vénere), feij@lncc.br (R.A. Feijóo).

0045-7825/$ - see front matter © 2005 Elsevier B.V. All rights reserved.
doi:10.1016/j.cma.2005.07.014

atherogenesis onset and progress [2] as low shear stress regions are associated with the development of stenotic plaques. Consequently, localized atherosclerotic lesions must be related to local flow conditions. Moreover, a deeper understanding and better descriptions of the flow structure in such a kind of vascular district ought to be of the greatest importance for the early detection of this type of arterial stenoses.

Several local 3D in vitro and computational flow models have been implemented, revealing the complex flow structure in the carotid sinus district. Bharadvaj et al. [37,38] defined a standard geometry of the carotid bifurcation (an average over 57 actual geometries from different subjects) and conducted stationary studies of the internal carotid blood flow. They found a region of low velocities near the non-dividing wall that extend with increasing Reynolds number. Conversely, the opposite region showed large axial velocities and shear stresses. These results were confirmed by Rindt et al. [3] using experimental and computational stationary models. Ku and Giddens [4–6] observed a similar process in 3D models during the accelerating period of the diastole and also, the existence of velocities disturbances during the decelerating phase and at the onset of the diastole. Some similar experiments have been conducted in compliant models [14].

To perform focused numerical and in vitro realistic experiments on a district such as the carotid bifurcation, special attention must be paid on the boundary conditions applied to the model. As the pressure differences between inlet and outlet boundaries are only a small percentage of the systolic-diastolic pulse amplitude, this imposes the problem of accurately determine the pressure, a condition that is difficult to reach in practice. In this way, small errors in the imposed pressure could lead to great departure of the velocities from the actual values. Conversely, if flow is imposed as boundary condition at the inlet and outlet of the analyzed zone, negligible variations on these values could lead to exaggerated low or high pressures. Accurate enough measures of those variables are very difficult or very costly to obtain simultaneously at the inflow and outflow regions for an entire cardiac period, even more in a non-invasive way. This in turn, leads to implement full models of the arterial tree in order to avoid artificial boundaries in the vicinity of the analyzed zone. Three-dimensional models of the whole arterial tree are, at the present times, not realizable as computational costs well exceed capabilities of modern computers and also, since it is a very compromised task to obtain and manage all the information (geometric and physiologic) necessary to construct such detailed models. Consequently, it is an interesting idea to model localized zones with great detail as 3D districts coupled with a 1D model—for the remaining part of the arterial tree—that serves as a boundary conditions provider to the former. This leads to a reduction in the number of parameters involved and also the overall complexity is substantially decreased.

Recently, the coupling and integration of models with different dimensionality have been analyzed by Quarteroni et al. [16–21], linking together lumped models with 3D models of the arterial tree. This task is very cumbersome since this problem involves deformable domains (compliant arterial walls) as well as other non-linearities in the governing equations such as convective terms, fluid–structure interactions and also, regions of diverse dimensionality and the coupling conditions between them. The authors have proposed elsewhere [11] an alternative approach for coupling models of non-matching dimensionality and used it to implement a model of stenoses in the common carotid artery. In this work, it is implemented a multidimensional 3D–1D model of the whole arterial tree which includes a 3D finite element model of the carotid bifurcation coupled with a 1D model for the remaining part of the arterial tree. Flow patterns for an entire cardiac period are obtained and analyzed in order to gain insight in the complexity of the unsteady flow in that region and also to evaluate the computational requirements for an accurate representation of the phenomena. Furthermore, flow rate and pressure curves at the inlet and outlet of the bifurcation are analyzed in order to show the compatibility of a pure 1D model with the coupled multidimensional model presented here.

2. The model

2.1. Governing equations

A compliant model of the whole arterial tree was developed. It comprises a 3D model of the carotid bifurcation embedded in a 1D representation for the rest of the arterial tree [12]. The governing equations for the 1D portion of the arterial system are derived from a reduced Navier–Stokes model. This leads to the following hyperbolic set of non-linear partial differential equations:

$$\frac{\partial Q}{\partial t} + \frac{\partial}{\partial x}\left(\alpha \frac{Q^2}{A}\right) = -\frac{A}{\rho}\frac{\partial P}{\partial x} - \frac{\pi D}{\rho}\tau_0, \tag{1}$$

$$\frac{\partial A}{\partial t} + \frac{\partial Q}{\partial x} = 0 \tag{2}$$

with

$$\alpha = \frac{\int_A u^2\,\mathrm{d}A}{Q^2}, \tag{3a}$$

$$\tau_0 = f_r \frac{\rho \tilde{u}|\tilde{u}|}{8}, \tag{3b}$$

$$Q = \tilde{u}A, \tag{3c}$$

where A is the artery cross sectional area, u the axial velocity ($\tilde{u}$ the corresponding mean value), x the axial coordinate, P the mean pressure, ρ the blood density, τ_0 the viscous shear stress acting on the arterial wall with f_r a Darcy friction factor (in this work a fully developed parabolic velocity profile is considered) and α is a correction factor for the axial momentum.

Taking into account the compliance of the arterial walls, a closure equation relating the pressure to the cross sectional area is implemented

$$P = P_0 + \frac{Eh_0}{R_0}\left(\sqrt{\frac{A}{A_0}} - 1\right), \tag{4}$$

where a linear relationship between P and R is considered, being R the radius of the artery, E an effective Young's modulus, h the thickness of the arterial wall and the subscript '0' denotes quantities evaluated at the reference pressure P_0.

The local 3D fluid dynamics was described using the 3D time-dependent Navier–Stokes equations for incompressible Newtonian fluids considering an A.L.E. method [32] in order to take into account the deformability of the domain. The governing equations are as follows:

$$\rho\frac{\partial \mathbf{u}}{\partial t} + \rho(\mathbf{u} - \mathbf{v})\nabla\mathbf{u} - \mu\nabla^2\mathbf{u} + \nabla P = \mathbf{f} \quad \text{in } \Omega, \tag{5a}$$

$$\operatorname{div}\mathbf{u} = 0 \quad \text{in } \Omega, \tag{5b}$$

$$\mathbf{u}(\mathbf{x}, t_0) = \hat{\mathbf{u}}(\mathbf{x}) \quad \text{in } \Omega, \tag{5c}$$

$$\mathbf{u}(\mathbf{x}, t) = \mathbf{v}_{\mathrm{w}}(\mathbf{x}, t) \quad \text{in } \Gamma_{\mathrm{w}}, \tag{5d}$$

where $\mathbf{u}$ is the fluid velocity, $\mathbf{v}$ is the moving reference frame velocity consistent with the A.L.E. formulation (and correspondingly, $\mathbf{v}_{\mathrm{w}}$ is the wall velocity), P is the pressure, $\mathbf{f}$ are the volume distributed forces, ρ and μ stand for the constant fluid density and the dynamic viscosity, respectively.

To obtain a field $\mathbf{v}$ corresponding to the velocity within the domain we solve a homogeneous Laplace problem for each displacement component, as stated by the following equation:

$$\nabla^2\Delta\mathbf{x} = 0 \quad \text{in } \Omega, \tag{6}$$

where $\Delta\mathbf{x}$ is the displacement vector of the moving domain from its reference configuration. The boundary conditions for these problems are given by

$$\Delta\mathbf{x} = \delta\mathbf{n} \quad \text{in } \Gamma_{\mathrm{w}} \tag{7a}$$

$$\nabla(\Delta\mathbf{x})\cdot\mathbf{n} = 0 \quad \text{in } \Gamma_i, \tag{7b}$$

$$P - P_0 = \frac{Eh}{R_0^2}\delta \quad \text{in } \Gamma_{\mathrm{w}} \tag{7c}$$

with $i = 1, \ldots, N_{\mathrm{cf}}$. Thus δ is the displacement of the arterial wall in the normal direction of the surface ($\mathbf{n}$ is the unit normal vector to the surface). Here, Eq. (7c) is analogous to that for the 1D model given in Eq. (4). In this way, the 3D model is provided with the simplest model for the arterial wall often called of "independent rings", in order to supply appropriate closure equations.

Consequently, the wall velocity $\mathbf{v}_{\mathrm{w}}$ is obtained from the time derivative of the displacement $\Delta\mathbf{x}$ at each point of the arterial wall Γ_{w} (see Eq. (7a) above).

2.2. Coupling conditions

Another group of equations must be considered to appropriately set the coupling between the 1D and the 3D models at the interface surfaces. To derive these coupling conditions, let us consider first a 1D segment divided into two parts, as shown in Fig. 1. In this case, flow continuity and pressure continuity arise as natural conditions at the interfaces in order to provide continuity to the relevant quantities. In view of that, we have

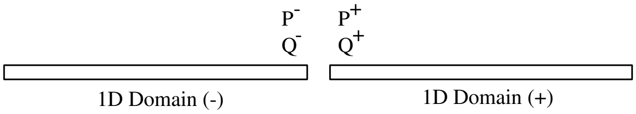

Fig. 1. Partition of the 1D model to set the coupling conditions.

$$P^- = P^+, \tag{8a}$$

$$Q^- = -Q^+. \tag{8b}$$

Observe that, area continuity is implicitly assured if both segments have the same constitutive law for the arterial wall.

Then, those coupling conditions must remain valid when substituting one of the 1D segments with a higher-dimensional model. On one hand, weak continuity on pressure at the interfaces of zones with different physical dimensions may be achieved by properly setting the Neumann boundary conditions within the variational formulation of the Navier–Stokes problem for the multidimensional domain (see Eq. (9)). In this way, using the pressure of the 1D model at the interfaces as Neumann boundary conditions in the variational formulation of the momentum equations for the multidimensional N–S problem we have

$$\begin{aligned}\int_\Omega \rho \frac{\partial \mathbf{u}}{\partial t} \cdot \mathbf{w}\, \mathrm{d}\Omega + \int_\Omega \rho(\mathbf{u}-\mathbf{v})\nabla\mathbf{u}\cdot\mathbf{w}\,\mathrm{d}\Omega - \int_\Omega P \,\operatorname{div}\mathbf{w}\,\mathrm{d}\Omega + \int_\Omega \mu\nabla\mathbf{u}\cdot\nabla\mathbf{w}\,\mathrm{d}\Omega \\ = -\sum_{i=1}^{N_{\mathrm{cf}}} \int_{\Gamma_i} P_i \mathbf{w}\cdot\mathbf{n}\,\mathrm{d}\Gamma_i + \int_\Omega \rho\mathbf{f}\cdot\mathbf{w}\,\mathrm{d}\Omega \quad \forall \mathbf{w}\in H(\Omega)^1,\end{aligned} \tag{9}$$

where Γ_i are the faces that are linked with a 1D model, N_{cf} is the number of coupling faces in the model, being P_i the mean pressure value as given by the 1D model at the coupling interface Γ_i. In this way, the corresponding Euler equation for the traction terms is consistent, in a weak sense as shown in Fig. 2, with:

$$P_i\mathbf{n} = \frac{1}{\mathrm{meas}(\Gamma_i)} \int_{\Gamma_i} (P\mathbf{n} - \mu\nabla\mathbf{u}\cdot\mathbf{n})_i \,\mathrm{d}\Gamma_i \quad \text{on } \Gamma_i,\ \ i = 1,\ldots,N_{\mathrm{cf}}. \tag{10}$$

Eq. (10) does not actually imply condition (8a), due to the term $\mu\nabla\mathbf{u}\cdot\mathbf{n}$. However, by finding the non-dimensional tensorial expression associated to Eq. (10),

$$P_i^*\delta_{\mathrm{km}} = \left(P^*\delta_{\mathrm{km}} - \frac{1}{Re}\frac{\partial u_k^*}{\partial x_m^*}\right)_i, \tag{11}$$

where the $*$ superscript means that the corresponding quantity is non-dimensional and δ_{km} is the Kronecker delta. It is easy to see that pressure continuity is achieved in the limit of high Reynold numbers (Re), a condition that is fulfilled for the flow regimes prevailing at the carotid artery.

On the other hand, an additional equation is required to impose flow continuity at each coupling face, resulting the following expression that satisfies condition (8b)

$$Q_i = -\int_{\Gamma_i} \mathbf{u}\cdot\mathbf{n}\,\mathrm{d}\Gamma_i \quad i = 1,\ldots,N_{\mathrm{cf}}. \tag{12}$$

The aim of the coupling scheme is to supply for the two subproblems (the 1D formulation and the corresponding for the 3D model) with appropriate boundary conditions in order to each subproblem result well posed from the point of view of a domain decomposition technique. It is worthwhile to note that, if we consider the problem splitted into two subproblems in the context of a domain decomposition strategy, the 1D model furnishes the multidimensional model with pressure boundary conditions on the coupling surfaces, whereas the multidimensional model imposes flow boundary conditions at the coupling points of the 1D model.

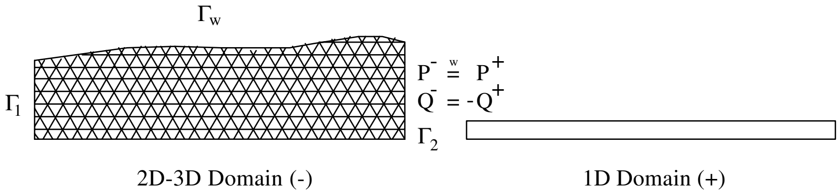

Fig. 2. Coupled system with a part replaced by a multidimensional model.

The resulting system of equations can be solved with a fully coupled scheme as well as with the mentioned subdomain strategy. In this work we have chosen the first alternative, although a subdomain decomposition may be useful as a preconditioner for the algebraic system of equations. The coupling strategy proposed here appears as a very simple and robust alternative to couple zones of diverse dimensionality in comparison with those proposed in [17], as they demand an impractible number of subrelaxation iterations for flow values within the physiological range [17]. In contrast, with the alternative proposed here no subrelaxation iterations were needed at all.

Observe that the number of unknowns associated to the 1D portion of the model are not significant when compared with the total number of unknowns. Furthermore, the 3D portion of the system is responsible for the major part of the computational costs, mainly due to its higher dimensionality. Notice that momentum continuity is implied in the correct choice of the parameter α in Eq. (3a), that must be evaluated non-linearly from the results of the 3D model. Here we have used $\alpha = 1$ constant. In this way the former requirement is not completely fulfilled, however, it must be noted that relaxing this condition does not produce significant spurious reflections in the case of long wavelengths, as is for the cases concerning this work.

3. Numerical approach

3.1. The 3D model

For the numerical solution of the 3D flow problem the finite element method was applied: the approximation makes use of P1–P1 bubble tetrahedral elements with linear enriched interpolation functions for the velocity vector field and linear pressure [15].

The equations are solved using the finite element SUPG [34] method with implicit Euler backward differences for time derivatives and Piccard iteration for non-linear convection terms. The solution of the time-dependent 3D Navier–Stokes equations is performed in two sub-steps: in the first one, the bubbles degrees of freedom are eliminated by direct substitution, and in the second one, those unknowns are updated as necessary for the evaluation of the second member of the first set of equations at the following time step. The deformation of the domain is accounted through a Laplace equation for the displacement of the mesh—again, tetrahedral linear elements are used—where boundary displacements at the arterial wall are given by Eq. (7c). The fluid–structure interaction problem concerning the arterial wall deformability is treated as fully coupled, regarding this issue, no stability problems were encountered along the numerical calculations. The backward Euler scheme used for time integration of the mesh movement does not satisfy the so called Geometric Conservation Law [22–25], so mass conservation is checked at the inlet and outlet interfaces of the 3D models.

Flow velocity patterns were calculated for a carotid artery bifurcation geometry proposed by Bharadvaj et al. [37,38] scaled to match the common carotid diameter of the 1D model (0.74 mm). The resulting geometry is shown in Fig. 3.

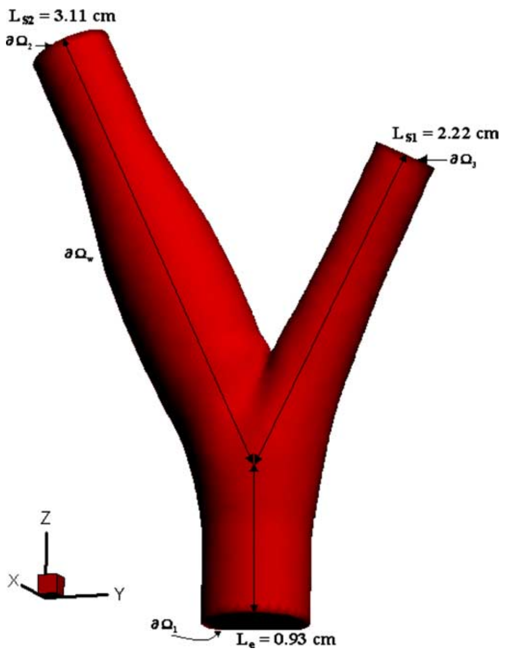

Fig. 3. 3D carotid bifurcation geometry model.

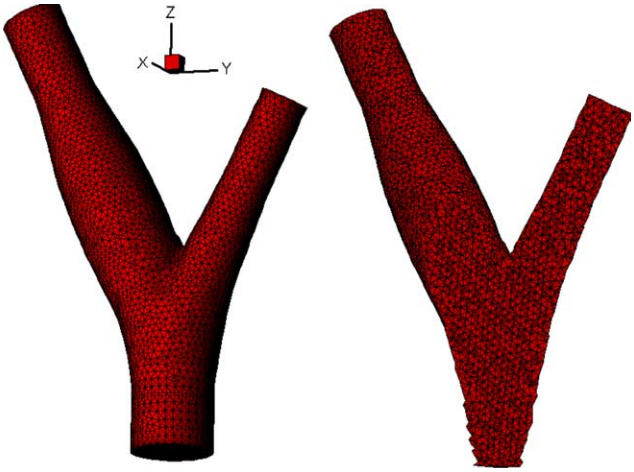

Fig. 4. 3D FEM mesh-tetrahedral elements.

The corresponding 3D mesh used in the calculations is exposed in Fig. 4, it has 14,159 nodes and 71,732 tetrahedral elements. With the simple wall model implemented it is possible to obtain self-intersecting surfaces for the deformed geometry at non-convex portions of the arterial wall. Although this is not a problem with the present numerical algorithm, it is not a realistic situation. But, also this issue could led to very badly shaped elements even with negative volume. To account for this potential problem the arterial wall was stiffened ten times for elements at the apex of the bifurcation. It is important to note that the present work is not concerned with the realistic representation of the arterial wall but with coupling compliant models of diverse dimensionality in an effective way.

3.2. The 1D model

Considering the corresponding eigenvalue problem for the 1D model, this system can be recasted in its canonical form along the characteristic lines [39,40], defined by the elastic propagation celerities (wave speeds), f^+ and f^-

$$\frac{\mathrm{D}Q}{\mathrm{D}t} - f^+\frac{\mathrm{D}A}{\mathrm{D}t} = g \quad \text{along} \quad \dot{x} = f^-(x(t),t), \tag{13a}$$

$$\frac{\mathrm{D}Q}{Dt} - f^-\frac{\mathrm{D}A}{\mathrm{D}t} = g \quad \text{along} \quad \dot{x} = f^+(x(t),t) \tag{13b}$$

with

$$g = -\frac{A}{\rho}\left(\frac{\partial P}{\partial \lambda_i}\frac{\partial \lambda_i}{\partial x} + \frac{f_r|\tilde{u}|Q}{4R}\right), \tag{14}$$

where λ_i are the parameters involved in the expression of P, such as A_0, E, etc. and

$$f^+ = \alpha\frac{Q}{A} + \sqrt{\alpha(\alpha-1)\frac{Q}{A} + \frac{A}{\rho}\frac{\partial P}{\partial A}}, \tag{15a}$$

$$f^- = \alpha\frac{Q}{A} - \sqrt{\alpha(\alpha-1)\frac{Q}{A} + \frac{A}{\rho}\frac{\partial P}{\partial A}}. \tag{15b}$$

When a numerical solution is attempted for the above problem (Eqs. (13)), the propagatory nature of the pulse waves must be taken into account, imposing the need of upwinding along the corresponding characteristic lines. In consequence, the numerical scheme is derived from a least squares form of the variational formulation. First, writing Eqs. (13) in their partial derivative form, we have

$$\frac{\partial Q}{\partial t} + f^-\frac{\partial Q}{\partial t} - f^+\left(\frac{\partial A}{\partial t} + f^-\frac{\partial A}{\partial t}\right) = g, \tag{16a}$$

$$\frac{\partial Q}{\partial t} + f^+\frac{\partial Q}{\partial t} - f^-\left(\frac{\partial A}{\partial t} + f^+\frac{\partial A}{\partial t}\right) = g. \tag{16b}$$

Then we proceed with time discretization as follows:

$$\frac{Q^{n+1}-Q^{n}}{\Delta t}+f^{-}\left.\frac{\partial Q}{\partial x}\right|_{n+\theta}-f^{+}\left(\frac{A^{n+1}-A^{n}}{\Delta t}+f^{-}\left.\frac{\partial A}{\partial x}\right|_{n+\theta}\right)=g^{n+\theta}, \tag{17a}$$

$$\frac{Q^{n+1}-Q^{n}}{\Delta t}+f^{+}\left.\frac{\partial Q}{\partial x}\right|_{n+\theta}-f^{-}\left(\frac{A^{n+1}-A^{n}}{\Delta t}+f^{+}\left.\frac{\partial A}{\partial x}\right|_{n+\theta}\right)=g^{n+\theta} \tag{17b}$$

with $\frac{1}{2}\leqslant\theta\leqslant 1$. After the introduction of standard linear C^0 finite element interpolation for the spatial variations of Q and A, two residuals are obtained

$$R^{-}=\frac{Q_i^{n+1}\phi_i-Q_i^{n}\phi_i}{\Delta t}+f^{-}\frac{\partial Q_i\phi_i}{\partial x}|_{n+\theta}-f^{+}\left(\frac{A_i^{n+1}\phi_i-A_i^{n}\phi_i}{\Delta t}+f^{-}\frac{\partial A_i\phi_i}{\partial x}|_{n+\theta}\right)-g^{n+\theta}, \tag{18a}$$

$$R^{+}=\frac{Q_i^{n+1}\phi_i-Q_i^{n}\phi_i}{\Delta t}+f^{+}\frac{\partial Q_i\phi_i}{\partial x}|_{n+\theta}-f^{-}\left(\frac{A_i^{n+1}\phi_i-A_i^{n}\phi_i}{\Delta t}+f^{+}\frac{\partial A_i\phi_i}{\partial x}|_{n+\theta}\right)-g^{n+\theta}. \tag{18b}$$

As mentioned, we obtain the set of equations by introducing a least squares technique, giving

$$\int_{\Omega}(R^{-}\mathscr{L}_Q^{-}+R^{+}\mathscr{L}_Q^{+})\,\mathrm{d}\Omega=0, \tag{19a}$$

$$\int_{\Omega}(R^{-}\mathscr{L}_A^{-}+R^{+}\mathscr{L}_A^{+})\,\mathrm{d}\Omega=0, \tag{19b}$$

where we have

$$\mathscr{L}_Q^{\mp}=\phi_j+f^{\mp}\tau^{\mp}\frac{\partial\phi_j}{\partial x}, \tag{20a}$$

$$\mathscr{L}_A^{\mp}=f^{\pm}\left(\phi_j+f^{\mp}\tau^{\mp}\frac{\partial\phi_j}{\partial x}\right). \tag{20b}$$

In the expressions (19) upwinding technique was performed, modifying the weighting functions as shown in Eqs. (20), where $\tau^{\mp}$ is the upwinding characteristic time.

With the proper choice of parameter $\tau^{\mp}$, Eqs. (19) may be alternatively considered as a least squares (LSFEM) formulation [41,42] or a Galerkin least squares (GLS) formulation [36], as indicated in the following equations:

$$\tau^{\mp}=\Delta t\rightarrow\text{LSFEM}, \tag{21a}$$

$$\tau^{\mp}=\frac{1}{2}\Delta x\ \text{sign}\{f^{\mp}\}\rightarrow\text{GLS}. \tag{21b}$$

Nevertheless, for Courant numbers close to unity both techniques have identical results for the tested cases.

The resulting algebraic system of equations is non-linear, thus Piccard iterations are employed to face this issue. The scheme is operated with $\theta=0.5$ and for a fixed time step, the element lengths are adjusted to get Courant number near to 0.85 at the beginning of the calculations.

In case of bifurcations and terminals, and even for the heart, it is implemented a Generic Windkessel element (see Fig. 6). These elements comprise $N_{\text{cs}}+1$ nodes, where N_{cs} is the number of concurrent segments to the bifurcation. Addi-

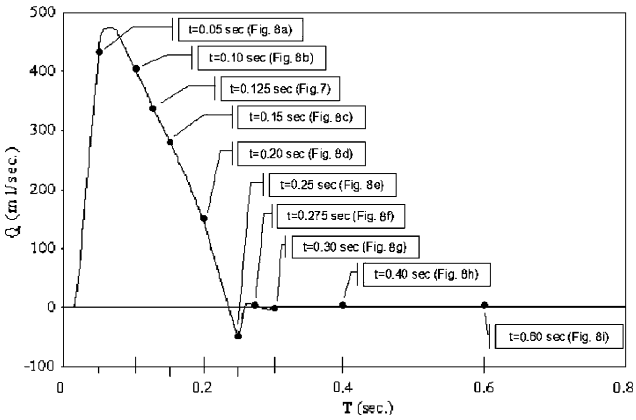

Fig. 5. Inflow boundary condition.

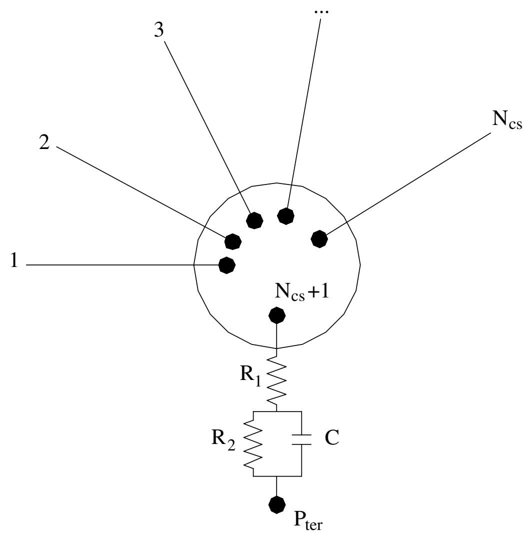

Fig. 6. A general Windkessel element.

tionally, a lumped branch is attached to these elements whose behavior are determined by a resistance R_1 in series with the parallel of a resistance R_2 and a capacitor C, the proper Windkessel terminal [30,31]. This element is used to implement all conditions on bifurcations and other singularities by means of setting element parameters as will be mentioned later in this section. The corresponding set of equations for a typical connection is as follows:

$$P_1 = P_i \quad i = 2, \ldots, N_{cs} + 1, \tag{22a}$$

$$\sum_{i=1}^{N_{cs}+1} Q_i = 0, \tag{22b}$$

$$\frac{dQ_{N_{cs}+1}}{dt} = \frac{1}{R_1 R_2 C}\left[R_2 C \frac{d\Delta P}{dt} + \Delta P - (R_1 + R_2) Q_{N_{cs}+1}\right], \tag{22c}$$

where $\Delta P = P_{N_{cs}+1} - P_{ter}$. The system of equations ensures pressure continuity as stated by Eq. (22a), blood flow conservation at the connection element (Eq. (22b)) with Eq. (22c) representing the Windkessel behavior of the attached lumped branch.

In this way, for a branch bifurcation the sum of R_1 and R_2 must tend to infinity in order to satisfy mass conservation between the concurrent segments. For pure terminals, the parameters determine the peripheral beds behavior and are obtained according to physiological data available, as shown in Table 1. Also, the inflow condition at the root of the aorta (heart ejection) can be modelled with this generic element as follows: consider a function $Q(t)$ representing the heart flow ejection that must be imposed as boundary condition at the entrance, see Fig. 5. Then, we can impose that flow curve by doing $P_{ter}(t) = (R_1 + R_2)Q(t)$, with $C = 0$, and setting $R_1 + R_2 \gg Z_0$, where Z_0 is the characteristic impedance of the aortic

Table 1
Windkessel terminals

No.	Name	R_1 (dyn s cm^{-2} ml^{-1})	R_2 (dyn s cm^{-2} ml^{-1})	C (ml cm^2 dyn^{-1})
1	Coronary	10.00E3	41.00E3	0.7900E−5
2	Intercostals	2.78E3	11.12E3	0.1638E−4
3	Gastric, hepatic and esplenic	2.54E3	10.17E3	0.2967E−3
4	Renal (two)	1.26E3	5.04E3	0.1235E−3
5	Superior mesenteric	1.92E3	7.68E3	0.1726E−3
6	Inferior mesenteric	16.62E3	66.46E3	0.7400E−4
7	Internal iliac	17.04E3	68.17E3	0.6750E−4
8	Deep femoral	11.60E3	46.39E3	0.5030E−5
9	Anterior tibial	56.15E3	224.61E3	0.4170E−5
10	Posterior tibial	9.54E3	38.16E3	0.3900E−5
11	Vertebral	16.65E3	66.60E3	0.9880E−4
12	Interosseous	211.74E3	846.96E3	0.3107E−6
13	Ulnar	10.56E3	42.24E3	0.3520E−5
14	Radial	10.56E3	42.24E3	0.3520E−5
15	Carotid	6.31E3	25.55E3	0.1330E−5

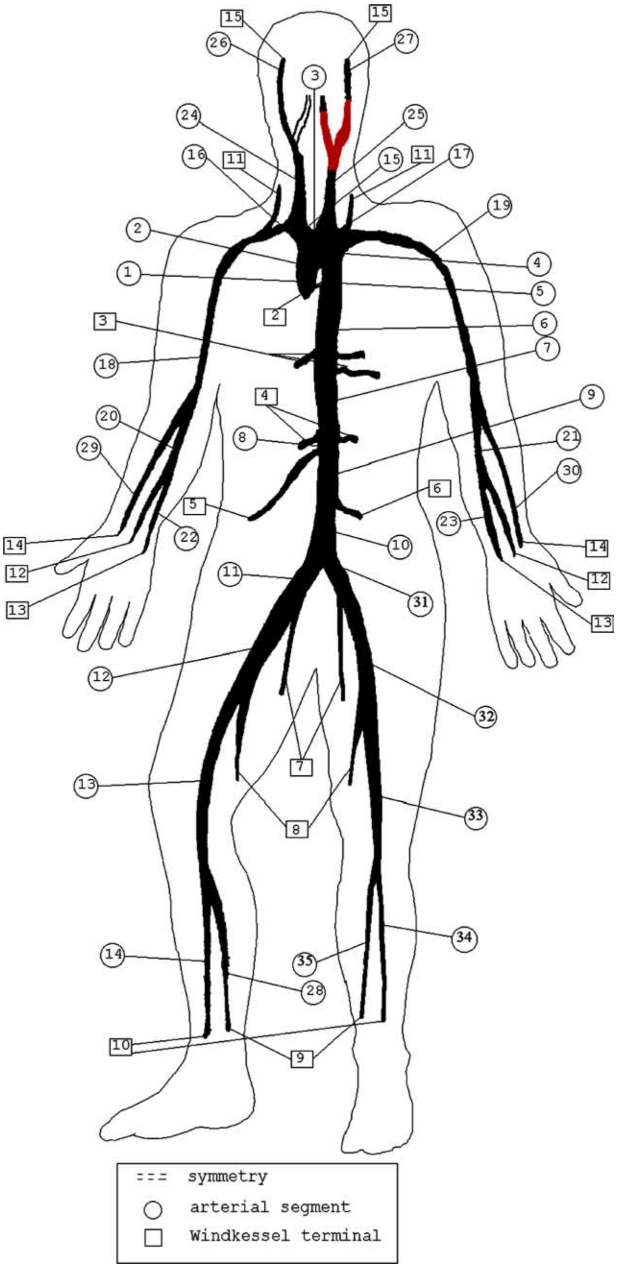

Fig. 7. Arterial tree scheme.

root. Therefore, with the proper choice of $P_{\mathrm{ter}}(t)$ and R_1, R_2 and C, any cardiac flow curve can be easily implemented as inflow boundary condition.

The geometry and other parameters involved in the calculations are shown in Fig. 7 and also in Tables 1 and 2. Some minor modifications are introduced here in order to match the diameters and lengths of the 1D model to those used in the 3D representation of the carotid bifurcation for the left external and internal carotid arteries. Finally, the selected values for ρ and μ were 1.04 g/cm^3 and 0.04 P respectively.

The resulting system of equations is discretized with a mesh comprising 686 nodes, 642 elements and considering three degrees of freedom per node (A, P, Q). The inlet boundary condition describing the heart blood flow is shown in Fig. 5 as previously mentioned, it has a period $t = 0.8$ s and was obtained from [26].

3.3. Implementation

The whole model was computationally implemented in a numerical framework [10] that allows to easily integrate different kinds of elements as “plug and play” without modifying the main program, i.e., the programmer only must provide

Table 2
Geometric and rheologic values of the arterial segments

No.	Name	Length (cm)	Proximal radius (cm)	Distal radius (cm)	Eh (dyn cm^{-1})
1	Ascending aorta A	1.0	1.46	1.46	741,500
2	Ascending aorta B	3.0	1.45	1.45	741,500
3	Aortic arch A	2.0	1.12	1.12	741,500
4	Aortic arch B	3.9	1.07	1.07	576,200
5	Thoracic aorta A	5.2	1.0	1.0	545,640
6	Thoracic aorta B	10.4	0.675	0.675	394,000
7	Abdominal aorta A	5.3	0.61	0.61	370,500
8	Abdominal aorta B and C	2.0	0.6	0.6	348,000
9	Abdominal aorta D	10.6	0.58	0.58	352,400
10	Abdominal aorta E	1.0	0.52	0.52	252,500
11, 31	Common iliac	5.8	0.37	0.37	368,150
12, 32	External iliac	14.4	0.32	0.32	148,700
13, 33	Femoral	44.3	0.26	0.26	230,900
14, 34	Posterior tibial	33.1	0.25	0.25	667,500
15	Innominate	3.4	0.62	0.62	377,000
16, 17	Subdavian A	3.4	0.423	0.423	288,700
18, 19	Subdavian B	42.2	0.403	0.403	1,170,000
20, 21	Ulnar A	6.7	0.215	0.215	679,100
22, 23	Ulnar B	17.1	0.203	0.203	717,664
24	Right common carotid	20.8	0.37	0.37	264,000
25	Left common carotid	19.87	0.37	0.37	264,000
26	Right external carotid	17.7	0.177	0.177	259,000
27	Left external carotid	15.48	0.21	0.21	302,504
28, 35	Anterior tibial	34.3	0.13	0.13	513,145
29, 30	Radial	23.5	0.174	0.174	682,580
36	Right internal carotid	17.7	0.177	0.177	259,000
37	Left internal carotid	14.59	0.2627	0.2627	378,130

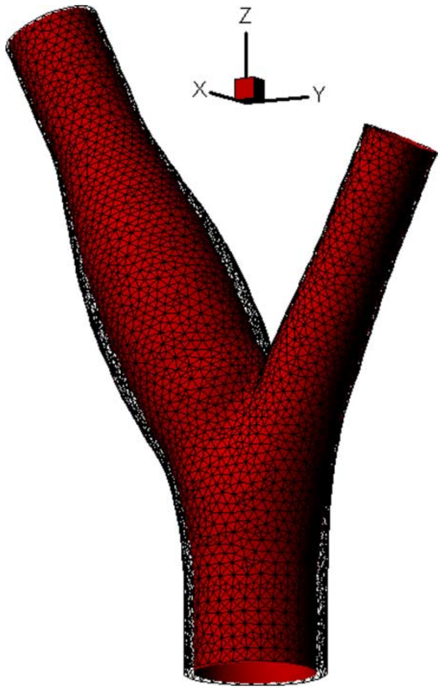

Fig. 8. Volume difference between systole and diastole.

the elemental matrices and organize the input in such a way that all run together. The linear equations are solved by a preconditioned (LU incomplete decomposition from SparseKit [9]) conjugated gradient square method [8], although similar performance can be obtained with BCG stabilized [9]. The cardiac period ($t = 0.8$ s) was divided into two subperiods.

For the systolic subperiod, a time step of 2.5E−3 s was used, and for the diastolic one was selected a time step of 5E−3 s. In this way, a very efficient and cost effective solver of the problem was implemented, making possible to obtain the results on a PC platform.

4. Results

Here we present some illustrative plots at selected times. In general, the flow has a very complex and unsteady structure showing an early back flow due to the inversion of the pressure gradient at the peak of the systole (Fig. 9).

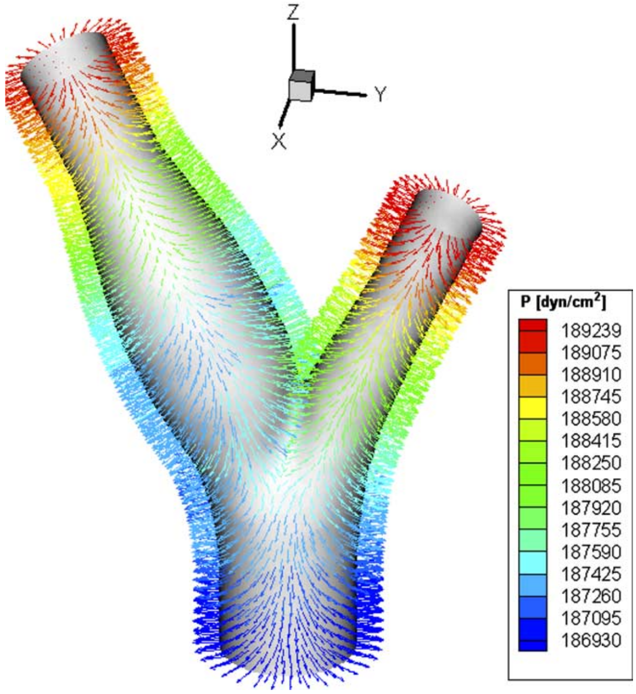

Fig. 9. Normal stress during systole at $t = 0.05$ s inverse pressure gradient.

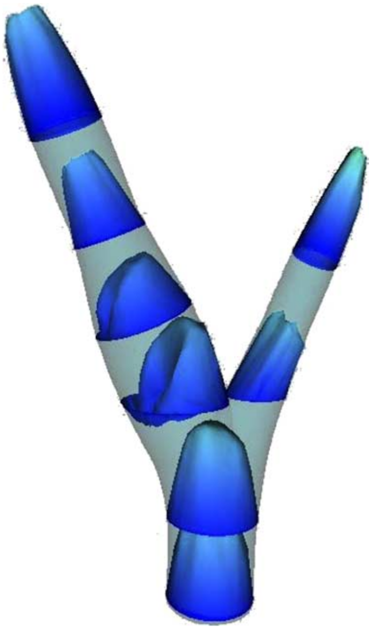

Fig. 10. Velocity during systole, $t = 0.125$ s.

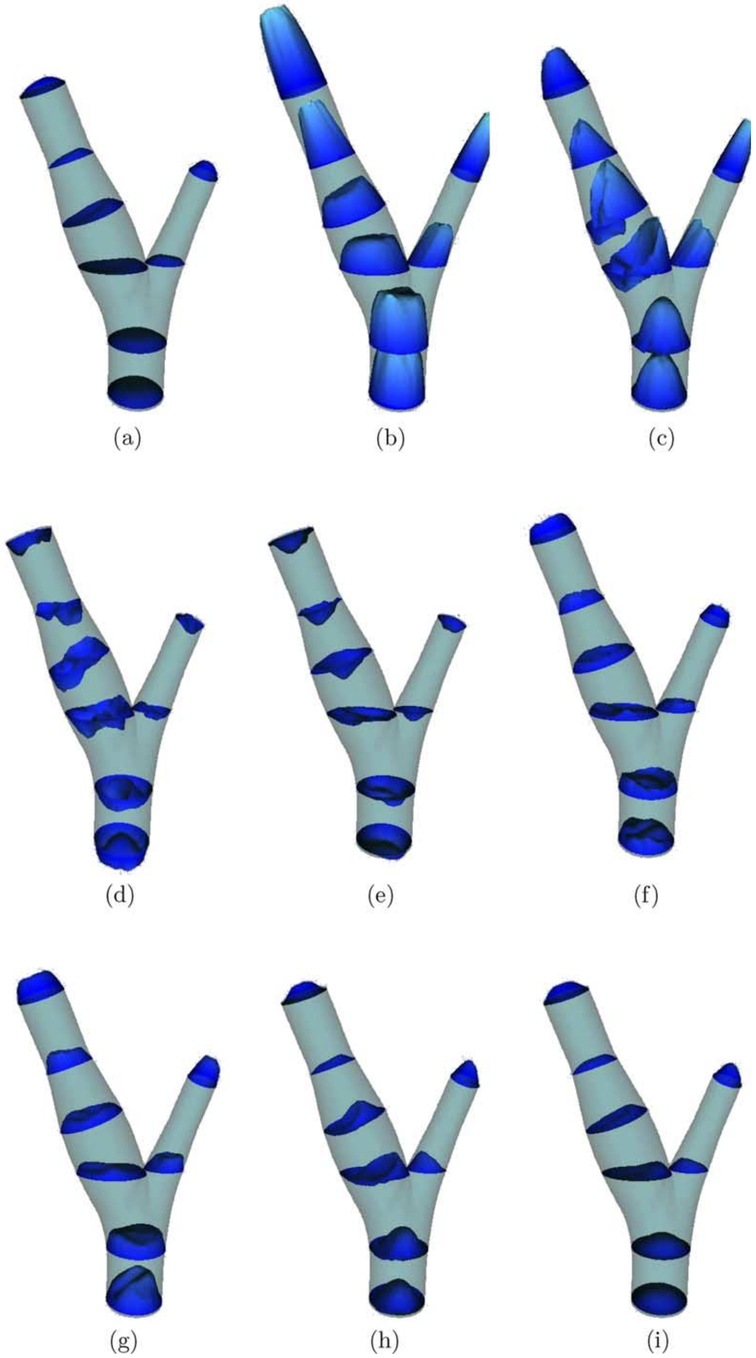

Fig. 11. Velocity profiles. (a) $t = 0.05$ s, (b) $t = 0.10$ s, (c) $t = 0.15$ s, (d) $t = 0.20$ s, (e) $t = 0.25$ s, (f) $t = 0.275$ s, (g) $t = 0.30$ s, (h) $t = 0.40$ s, (i) $t = 0.60$ s.

A considerable deformation of the artery volume can be observed in Fig. 8 where volume differences during diastole (red shaded[1]) and systole (black wire frame) are displayed.

As can be seen in Fig. 10, a zone of low velocities near the non-divider wall of the carotid sinus is observed and contrariwise, a high velocity region occurs near the divider wall. These results agree with those obtained experimentally and numerically in Refs. [7,14,37,38]. Detailed inspection of the computational results (see Fig. 11(a)–(i)) displays the general characteristics occurring in the carotid sinus, a period with reverse axial flow starts at the peak of the systole and remains until the beginning of the diastole. This is illustrated for the V_z component of the velocity vector during the decreasing phase of the systole as shown in Fig. 12. Also in that figure can be observed a typical Womersley flow at the entrance, where

---

[1] For interpretation of the references in colour in this figure legend, the reader is referred to the web version of this article.

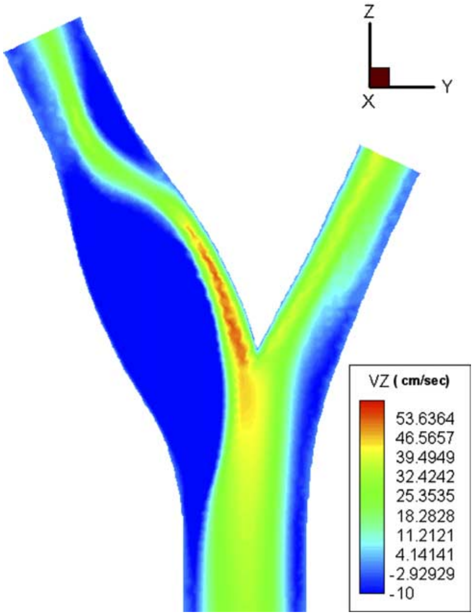

Fig. 12. Back flow during late systole, $t = 0.18$ s.

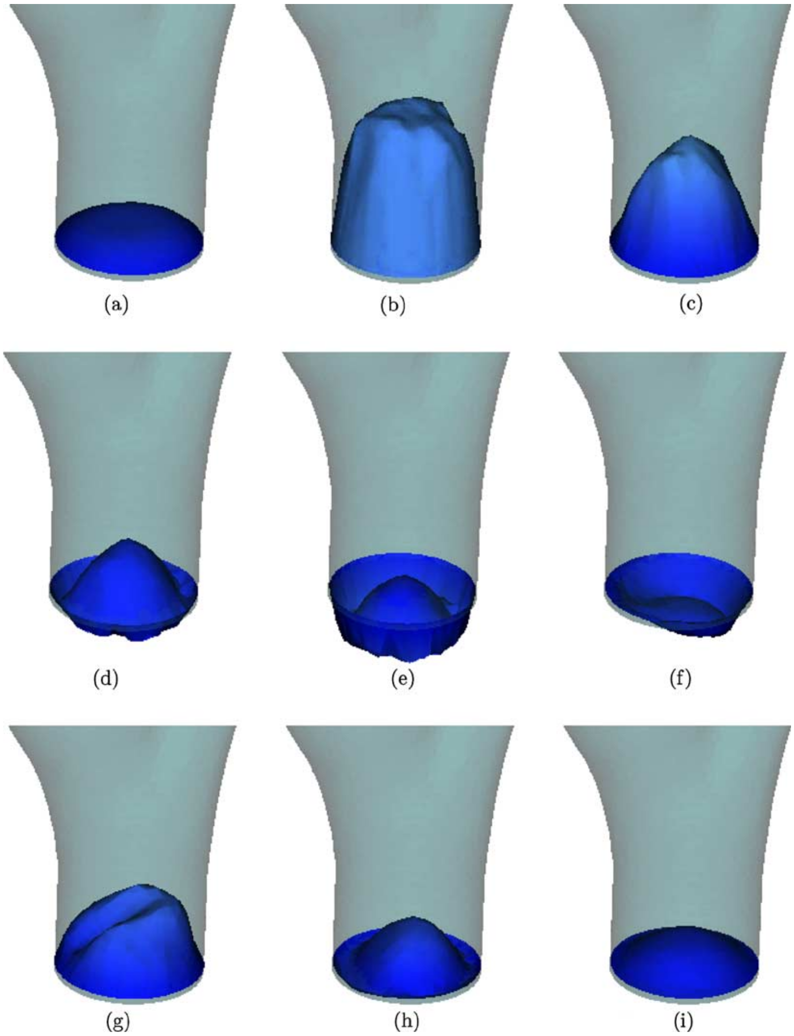

Fig. 13. Velocity profiles at the entrance of the common carotid. (a) $t = 0.05$ s, (b) $t = 0.10$ s, (c) $t = 0.15$ s, (d) $t = 0.18$ s, (e) $t = 0.20$ s, (f) $t = 0.25$ s, (g) $t = 0.30$ s, (h) $t = 0.40$ s, (i) $t = 0.60$ s.

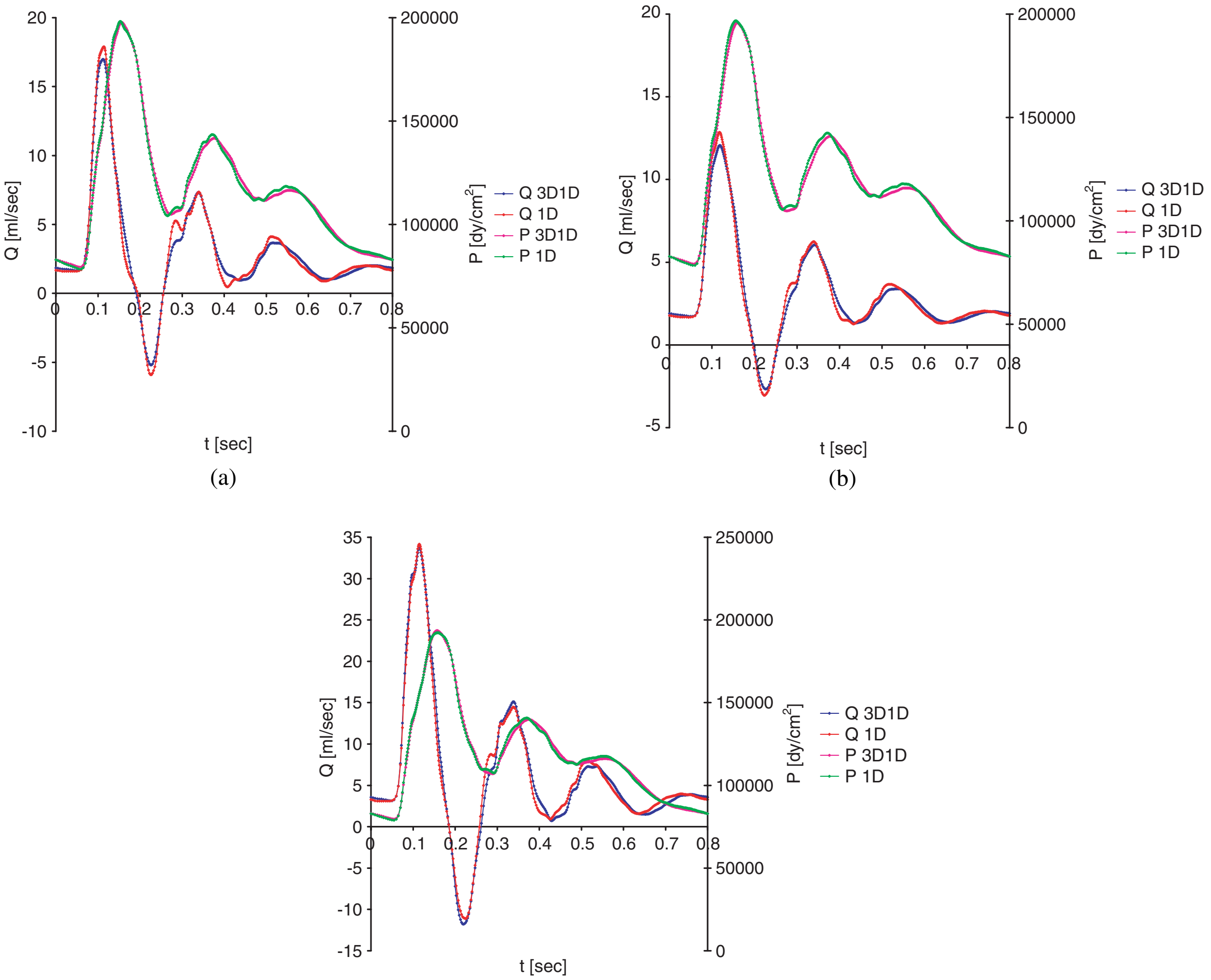

(a) (b)

(c)

Fig. 14. Flow rate and pressure curves at the interfaces. (a) Major outlet, (b) minor outlet, (c) inlet.

the flow reversal occurs at the outer ring while at the center the velocity remains positive. In Fig. 13(a)–(i) the obtained computational velocity profiles at the entrance of the common carotid are presented.

Also the outflow velocity profile for the internal and external carotid was integrated over the duration of the cardiac cycle and compared with that for the inflow condition, resulting in a conservation of mass higher than the 99.5%.

With the aim of examining the consistency of the multidimensional coupled model with regard to a pure 1D model, flow rate and pressure curves are compared. This is carried out by plotting results at the inlet and at the outlets of the 3D districts. Fig. 14c shows those quantities for the inlet, whereas Fig. 14(a) and (b) shows the same for both outlets. Also from these plots, the non-dimensional L^2 norm for the differences between values corresponding to the coupled model and the pure 1D model was evaluated, resulting in errors lower than 2% for all cases.

In this point, it is important to mention that the influence of a parietal viscoelastic behavior is under analysis in order to reproduce real flow curves at the common carotid artery. Likewise, the implementation of non-Newtonian models is being studied so as to determine changes in the flow structure at the carotid sinus.

5. Conclusions

A computational model that face the problem of simulating compliant 3D arterial districts coupled with a 1D model of the rest of the arterial tree was presented. The resulting scheme has shown excellent capabilities to deal with considerable domain deformations while preserving the computational efficiency. Calculations of the flow field for the carotid artery are in general agreement with those reported previously in the literature, for both experimental and numerical cases [5–7,14,27]. The consistency of the coupled model was also shown by computing flow rate and pressure curves at the coupling boundaries and comparing these results with those of a pure 1D model. Finally, this class of model can be of valuable aid as it takes into account more realistic boundary conditions when studying 3D zones of the arterial tree, a fact that can contribute to gain insight on the flow patterns that influence the start and development of atherosclerotic disease.

Acknowledgements

This research was partly supported by FINEP/CNPq-PRONEX Project under Contract 664007/1997-0, by MCT/PCI-LNCC Project, CNPq-Grant 304850/2003-9 and by CONICET (Argentina). Pablo Javier Blanco was partly supported by the Brazilian agency CNPq. The support from these agencies is greatly appreciated.

References

[1] P. Bruinsma, T. Arts, J. Dankelman, J.A.E. Spaan, Model of the coronary circulation based on pressure dependence of coronary resistance and compliance, Basic Res. Cardiol. 83 (1988) 510–524.

[2] C.G. Caro, J.M. Fitz-Gerald, R.C. Schroter, Atheroma and arterial wall shear dependent mass transfer mechanism for atherogenesis, Proc. Roy. Soc. Lond. Biol. B 177 (1971) 109–159.

[3] C.C.M. Rindt, A.A. Steenhoven, J.D. Van Janssen, R.S. Reneman, A. Segal, A numerical analysis of steady flow in a three-dimensional model of the carotid artery bifurcation, J. Biomech. 23 (1990) 461–473.

[4] D.N. Ku, D.P. Giddens, Hemodynamics of the normal carotid bifurcation, Ultrasound Med. Biol. 11 (1985) 13–26.

[5] D.N. Ku, D.P. Giddens, Laser Doppler anemometer measurements of pulsatile flow in a model carotid bifurcation, J. Biomech. 20 (1987) 407–421.

[6] D.N. Ku, D.P. Giddens, C.K. Zarins, S. Glagov, Pulsatile flow and atherosclerosis in the human carotid bifurcation, Arteriosclerosis 5 (1985) 293–302.

[7] R.H. Botnar, G. Rappitsch, M.B. Scheidegger, D. Liepsch, K. Perktold, P. Boesiger, Hemodynamics in the carotid artery bifurcation: a comparison between numerical simulations and in vitro MRI measurements, J. Biomech. 33 (2000) 137–144.

[8] P. Sonneveld et al., Multigrid and conjugate gradient methods as convergence acceleration techniquesMultigrid Methods in Integral Differential Equations, Clarendon Press, Oxford, 1985.

[9] Y. Saad, SPARSEKIT: a basic tool kit for sparse matrix computation version 2, Available from: <http//:www-users.cs.umn.edu/~saad/software/SPARSEKIT/sparsekit.html>, University of Illinois, 1985.

[10] S.A. Urquiza, M.J. Vénere, An application framework architecture for FEM and other related solvers, in: S. Idelsohn, V. Sonzogni, A. Cardona (Eds.), Mecánica Computacional, vol. XXI, CERIDE, Santa Fe, 2002, pp. 3099–3109.

[11] S.A. Urquiza, A.L. Reutemann, M.J. Vénere, R.A. Feijóo, Acoplamiento de modelos unidimensionales y multidimensionales para la resolución de problemas hemodinámicos, in: Proc. ENIEF 2001, XII Congress on Numerical Methods and Their Applications, AMCA, Córdoba, 2002.

[12] S.A. Urquiza, M.J. Vénere, F.M. Clara, R.A. Feijóo, Finite element (one-dimensional) hemodynamic model of the human arterial system, in: E. Onate, G. Bugeda, B. Suarez, (Eds.), Proc. ECCOMAS 2000, European Community on Computational Methods in Applied Sciences and Engineering, Artes Gráficas Torres S.A., Barcelona, 2000.

[13] D.P. Giddens, C.K. Zarins, S. Glagov, The role of fluid mechanics in the localization and detection of atherosclerosis, J. Biomech. Engrg. 115 (1993) 588–594.

[14] A.S. Anayiotos, S.A. Jones, D.P. Giddens, S. Glagov, C.K. Zarins, Shear stress at a compliant model of the human carotid bifurcation, J. Biomech. Engng. 117 (1994) 98–106.

[15] O. Pironneau, Finite Element Methods for Fluids, Wiley, New York, 1989.

[16] A. Quarteroni, Modelling the cardiovascular system: a mathematical challenge, in: B. Engquist, W. Schmid (Eds.), Mathematics Unlimited—2001 and Beyond, Springer-Verlag, Berlin, 2001, pp. 961–972.

[17] L. Formaggia, J.F. Gerbeau, F. Nobile, A. Quarteroni, On the coupling of 3D and 1D Navier–Stokes equations for flow problems in compliant vessels, Comput. Methods Appl. Mech. Engrg. 191 (2001) 561–582.

[18] L. Formaggia, J.F. Gerbeau, F. Nobile, A. Quarteroni, Numerical treatment of defective boundary conditions for the Navier–Stokes equations, SIAM J. Numer. Anal. 40 (2002) 376–401.

[19] R. Pietrabissa, A. Quarteroni, G. Dubini, A. Veneziani, F. Migliavacca, S. Ragni, From the global cardiovascular hemodynamics down to the local blood motion: preliminary applications of a multiscale approach, in: E. Oate, G. Bugeda, B. Suarez, (Eds.), Proc. ECCOMAS 2000, European Community on Computational Methods in Applied Sciences and Engineering, Artes Gráficas Torres S.A., Barcelona, 2000.

[20] A. Quarteroni, M. Tuveri, A. Veneziani, Computational vascular fluid dynamics: problems, models and methods, Comput. Visual. Sci. 2 (2000) 163–197.

[21] L. Formaggia, F. Nobile, A. Quarteroni, A. Veneziani, Multiscale modelling of the circulatory system: a preliminary analysis, Comput. Visual. Sci. 2 (1999) 75–83.

[22] F. Nobile, Numerical approximation of fluid–structure interaction problems with application to haemodynamics, Ph.D. Thesis, Report Number 2458, EPFL, Lausanne, 2001.

[23] H. Guillard, C. Farhat, On the significance of the geometric conservation law for computations on moving meshes, Comput. Methods Appl. Mech. Engrg. 190 (2000) 1467–1482.

[24] B. Koobus, C. Farhat, Second-order time-accurate and geometrically conservative implicit schemes for computations on unstructured dynamic meshes, Comput. Methods Appl. Mech. Engrg. 170 (1999) 103–129.

[25] M. Lesoinne, C. Farhat, Geometric conservation laws for aeroelastic computations using unstructured dynamics meshes, in: 12th AIAA Computational Fluid Dynamics Conference (AIAA-95-1709, San Diego, June 1995).

[26] J.C. Stettler, P. Niederer, M. Anliker, Theoretical analysis of arterial hemodynamics including the influence of bifurcations part I, Ann. Biomed. Engrg. 9 (1981) 145–164.

[27] K. Perktold, G. Rappitsch, Computer simulation of local blood flow and vessel mechanics in a compliant carotid artery bifurcation model, J. Biomech. 28 (1995) 845–856.

[28] M.F. Snyder, V.C. Rideout, R.J. Hillestad, Computer modelling of the human systemic arterial tree, J. Biomech. Engrg. 1 (1968) 341–353.

[29] A.P. Avolio, Multi-branched model of the human arterial system, Med. Biol. Engrg. Comput. 18 (1980) 709–718.

[30] N. Stergiopulos, D.F. Young, T.R. Rogge, Computer simulation of arterial flow with applications to arterial and aortic stenoses, J. Biomech. 25 (1992) 1477–1488.
[31] B.W. Schaaf, P.H. Abrecht, Digital computer simulation of human systemic arterial pulse wave transmission: a nonlinear model, J. Biomech. Engrg. 15 (1982) 349–362.
[32] T.J.R. Hughes, W.K. Liu, T.K. Zimmermann, Lagrangian–Eulerian finite element formulation for incompressible viscous flows, Comput. Methods Appl. Mech. Engrg. 29 (1981) 329–349.
[33] T.J.R. Hughes, A study of the one-dimensional theory of arterial pulse propagation, Ph.D. Thesis, Report Number 74-13, Structures and Materials Research, Department of Civil Engineering, Division of Structural Engineering and Structural Mechanics, University of California, Berkeley, 1974.
[34] T.J.R. Hughes, A. Brooks, A theoretical framework for Petrov–Galerkin methods with discontinuous functions: Application to the stream-upwind procedure, in: R.H. Gallagher, D.M. Norrie, J.T. Oden, O.C. Zienkiewicz (Eds.), Finite Element in Fluids, col. IV, Wiley, London, 1982, pp. 46–65.
[35] C.A. Taylor, T.J.R. Hughes, C.K. Zarins, Finite element blood flow modeling in arteries, Comput. Methods Appl. Mech. Engrg. 158 (1998) 155–196.
[36] T.J.R. Hughes, L.P. Franca, G.M. Hulbert, A new finite element formulation for computational fluid dynamics: VIII. The Galerkin/least squares method for advective–diffusive equations, Comput. Methods Appl. Mech. Engrg. 73 (1989) 173–189.
[37] B.K. Bharadvaj, R.F. Mabon, D.P. Giddens, Steady flow in a model of the human carotid bifurcation—I. Flow visualisation, J. Biomech. 15 (1982) 349–362.
[38] B.K. Bharadvaj, R.F. Mabon, D.P. Giddens, Steady flow in a model of the human carotid bifurcation—II. Laser-Doppler anemometer measurements, J. Biomech. 15 (1982) 363–378.
[39] R.D. Richtmyer, K.W. Morton, Difference Methods for Initial-Value Problems, Interscience Publishers, New York, 1967.
[40] R. Courant, D. Hilbert, Methods of Mathematical Physics, vol. II, Interscience Publisher, New York, 1962.
[41] G.F. Carey, B.N. Jiang, Least squares finite elements for first-order hyperbolic systems, Int. J. Numer. Methods Fluids 26 (1988) 81–93.
[42] B.N. Young, G.F. Carey, A stable least-squares FEM for non-linear hyperbolic problems, Int. J. Numer. Methods Fluids 8 (1988) 933–942.